

Enhancing Positron Production using Front Surface Target Structures

Sheng Jiang (✉ jiang8@llnl.gov)

Lawrence Livermore National Laboratory <https://orcid.org/0000-0002-0381-3846>

Anthony Link

LLNL

Dave Canning

Laboratory For Laser Energetics

Julie Fooks

General Atomics

Paul Kempler

California Institute of Technology

Shaun Kerr

Lawrence Livermore National Laboratory

J Kim

University of California, San Diego

Michael Krieger

Laboratory For Laser Energetics

Nathan Lewis

California Institute of Technology

Russell Wallace

LLNL

G. Jackson Williams

Lawrence Livermore National Laboratory <https://orcid.org/0000-0002-6495-5696>

Sisir Yalamanchili

California Institute of Technology

Hui Chen

Lawrence Livermore National Laboratory

Article

Keywords: positrons, laser, plasma, front-surface target structures

Posted Date: August 21st, 2020

DOI: <https://doi.org/10.21203/rs.3.rs-53834/v1>

License:   This work is licensed under a Creative Commons Attribution 4.0 International License.

[Read Full License](#)

Enhancing Positron Production using Front Surface Target Structures

S. Jiang¹, A. Link¹, D. Canning², J. A. Fooks³, P. A. Kempler⁴, S. Kerr¹, J. Kim⁵, M. Krieger², N. S. Lewis⁴, R. Wallace¹, G. J. Williams¹, S. Yalamanchili⁴ & H. Chen¹

¹*Lawrence Livermore National Laboratory, Livermore, California, USA*

²*Laboratory For Laser Energetics, Rochester, New York, USA*

³*General Atomics, San Diego, California, USA*

⁴*California Institute of Technology, Pasadena, California, USA*

⁵*Center for Energy Research, University of California San Diego, San Diego, California, USA*

We report the first experimental results and simulations that demonstrate a substantial effect of large-scale front-surface target structures on high-intensity laser-produced positrons. Specifically, as compared to a flat target under nominally the same laser conditions, an optimized Si microwire array target yielded a near 100% increase in the laser-to-positron conversion efficiency and produced a 10 MeV increase in positron energy. Full-scale particle-in-cell simulations that modeled the entire positron production and transport process starting from laser-plasma interactions provided additional insight into the beneficial role of target structuring. The agreement between experimental and simulated spectra suggests future target structure optimization for desired positron sources.

Electron-positron pair plasmas are found in various extreme astrophysical objects, such as pulsars, bipolar outflows, active galactic nuclei, and gamma ray bursts¹. Producing a pair plasma

21 with similar conditions in the laboratory is extremely challenging but could significantly deepen
22 the understanding of these exotic objects ²⁻⁵. With the advances in high intensity laser technol-
23 ogy, several methods for pair production have been either demonstrated or proposed, with differ-
24 ent mechanisms dominating the physics in different regimes of laser intensity. For example, the
25 Schwinger mechanism ⁶ requires an extremely high intensity, above $\sim 10^{29}$ W/cm², for sponta-
26 neous pair creation from vacuum, whereas the Breit-Wheeler (BW) mechanism ⁷ requires about
27 10^{25} W/cm² for avalanche-type discharge ⁸. These intensities are far beyond the capability of
28 state-of-the-art lasers (up to 10^{22} W/cm²).

29 An alternative method is to inject laser produced high-energy electrons into high-Z target
30 materials ^{4,9-15}, with the electrostatic field of the nucleus involved in the pair production process
31 releasing the constraint on the laser E field intensity. As these high-energy electrons transport
32 through the material, positrons are produced via two major mechanisms: the trident process and
33 the Bethe-Heitler (BH) process ¹⁶. The latter process dominates when a thick target is used. In
34 a laser experiment, pair production via the BH process includes three steps. First, relativistic
35 electrons are generated through a laser plasma interaction (LPI) at the front side of the target.
36 These electrons then transport through the high-Z material and produce high-energy photons via
37 Bremsstrahlung radiation. Retardation of the high-energy photons in the field of nucleus then
38 creates electron-positron pairs. The key step is to transfer laser energy into enough high-energy
39 (10s of MeV) electrons, for which, only a moderate intensity laser ($\sim 10^{20}$ W/cm²) is needed.
40 Experiments using this type of setup have produced up to 10^{12} pairs/shot, which is the highest
41 yield reported to date by use of lasers.

42 Optimizing the positron yield is critical to apply the laser-produced pairs to laboratory astro-
43 physics. Although higher laser intensities or energies can produce a larger pair yield, at present,
44 improvements are needed before lasers can provide enough power to permit scaled laboratory as-
45 trophysics experiments.

46 The electron temperature largely determines the positron yield from the BH mechanism, so a
47 key to higher positron production is the production of hotter electrons. In addition to increasing the
48 laser intensity, substantial enhancement in electron energies can be obtained by manipulating the
49 laser-plasma interaction using a structured front surface target ^{17,18}. Specifically, highly-ordered
50 silicon microwire arrays facing the laser pulse enable guiding the relativistic electron beam along
51 the structured surface and moreover facilitate a direct laser acceleration mechanism. Such an
52 electron beam can then create a substantial enhancement in the Bremsstrahlung radiation produced
53 by a high-Z converter target ¹⁹. The Bremsstrahlung x-rays further interact with atomic nuclei in
54 the converter target and create more electron-positron pairs through the BH process.

55 We demonstrate herein experimentally a substantial enhancement in both the yield and the
56 energy of generated positrons using target structures, which suggests an efficient and inexpensive
57 approach to improvement of positron sources. Particle-in-cell (PIC) simulations with the code
58 Chicago ²⁰ have been used to explain the experimental results and have allowed a direct simulation
59 of the effects of the laser-plasma interaction (LPI) on the positron yield. Moreover, the simulation
60 is in good qualitative agreement with the experimental data.

61 Results

62 **Experiment.** A schematic diagram of the experimental setup is shown in Figure 1(a). The struc-
63 tured target was irradiated with the OMEGA EP laser pulse, with a wavelength of $1.053 \mu\text{m}$, an
64 energy of 500 J, and a pulse length of approximately 700 fs. The focal spot at the target was about
65 $30\mu\text{m}$ in diameter as derived from an on-shot wavefront and far-field measurement. The peak
66 intensity was therefore estimated to be $4.5 \times 10^{20} \text{ W/cm}^2$. Prior to the experiment, the structure
67 geometry (spacing and length) was optimized through PIC simulations of the hot electron temper-
68 ature. The optimal geometry is an array of silicon microwires with $3 \mu\text{m}$ diameter, $13 \mu\text{m}$ length
69 and $15 \mu\text{m}$ center-to-center transverse distance. For reference, we have also shot flat targets as
70 well as another type of unoptimized control structure that showed detrimental effects on electron
71 energies in simulations. The second type of target had $3 \mu\text{m}$ diameter, $100 \mu\text{m}$ length and $7 \mu\text{m}$
72 center-to-center transverse distance. The microwires in the latter target have been shown in previ-
73 ous work to be too long in length and too close to each other, so they tend to break the laser pulse
74 and consequently lead to a poor electron spectrum^{17,18}.

75 Figure 1(b) and (c) show scanning electron microscope images of both target structures used
76 in the experiment. The Si microwire arrays $100 \mu\text{m}$ in height were first grown on a Si $\langle 111 \rangle$
77 wafer by the vapor-liquid-solid growth method²¹, whereas the shorter, optimal microwire arrays
78 were etched from Si $\langle 100 \rangle$ wafers via Deep Reactive Ion Etching²². The microwires were then
79 embedded in a $\sim 30 \mu\text{m}$ thick polydimethylsiloxane layer and peeled off of the substrate. This thin
80 polydimethylsiloxane layer was then attached to a 1mm thick Au backing layer. In this case, the

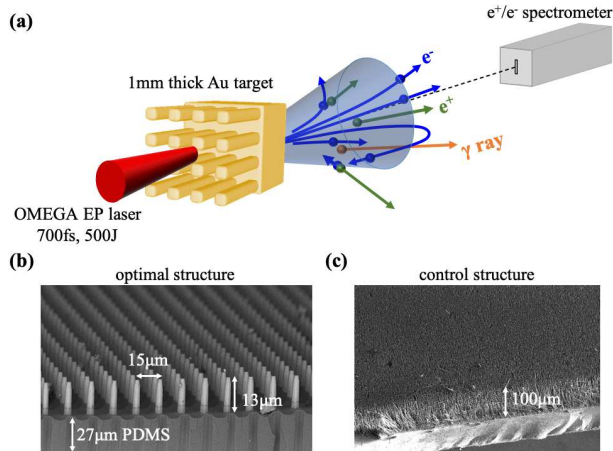


Figure 1: Schematic diagram of the experimental setup and scanning electron microscope (SEM) images of targets. (a) Schematic of the experimental setup. The same setup is used for LPI PIC simulations. The laser has 500 J energy, 700 fs pulse length and a peak intensity of 4.46×10^{20} W/cm². Target structures are made of Si wires that reside on a thin piece of polydimethylsiloxane. They are then attached to a 1mm thick Au convertor target for positron generation. The electron/positron spectrometer is placed opposite to the laser pulse. (b) SEM image of the optimized target structure. The wires are 3 μm in diameter and 15 μm apart. They have a total length of 40 μm but their bottom parts are embedded inside a 27 μm polydimethylsiloxane layer; therefore the wire structures exposed outside the polydimethylsiloxane is 13 μm . (c) SEM image of the unoptimized control structure used in the experiment. The Si wire array is about 100 μm long (exposed outside polydimethylsiloxane), 3 μm in diameter, and 7 μm in period.

81 high-energy electrons generated and guided by the surface structures would transport through a
 82 thick high-Z material (Au) and induce pair production. The transverse size of the Au block used
 83 in the experiment was also 1mm. The laser was directed at normal incidence onto the target and
 84 the microwire arrays were oriented along the laser direction. This configuration has been shown
 85 in previous work to yield the highest enhancement of electron energy and directionality^{17,18}. The
 86 positron spectra were measured by an electron/positron spectrometer on the back side of the target
 87 along the laser direction (which was also the target normal direction).

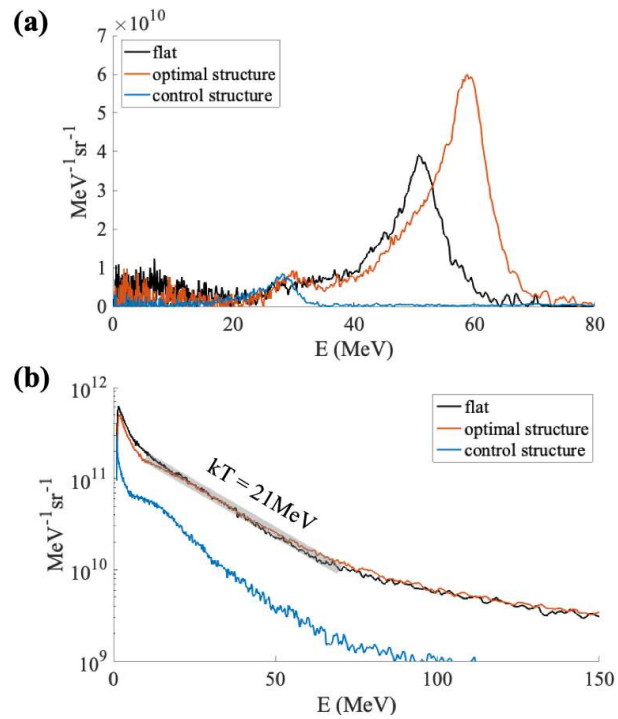


Figure 2: Experimentally measured spectra for (a) positrons and (b) electrons. Different colors indicate the results from different targets under the same laser conditions.

88 The experimental positron and electron spectra for 3 different types of targets are shown in
 89 Figure 2(a) and (b). The optimally structured target generated about 50% more positrons than the

90 regular flat target, and the laser to positron conversion efficiency doubled for the optimal structure
91 compared to the flat substrate. The spectrum peak also shifted from ~ 50 MeV for the flat target
92 to ~ 60 MeV for the optimally structured target. The unoptimized structure showed fewer as well
93 as much lower-energy positrons, in accord with expectations. The electron spectrum from the
94 unoptimized structure also showed the same trend, in agreement with the positron measurements.
95 However, the electron spectra from flat and optimally structured targets were mutually similar,
96 with both having an electron temperature of about 21 MeV.

97 **Simulations and Discussions** Multiple simulations to model the entire process were performed
98 to elucidate why the measured positron spectrum from optimal structure is obviously superior
99 while its electron spectrum is similar to that from flat target. The simulations used the same laser
100 conditions and target geometries as the experiment. We fitted the measured laser fluence map with
101 two Gaussian functions to maintain the intensity distribution of the experiment. The OMEGA EP
102 laser had a substantial prepulse that could affect the conversion efficiency from the laser to fast
103 electrons, and would therefore affect the yield and energy of positrons. The facility has an on-shot
104 prepulse measurement from 3 ns to 1 ns prior to the main laser pulse. For the prepulse within 1 ns,
105 we assumed a similar profile to that measured by Dorrer et al. on OMEGA EP²³. The total energy
106 of the prepulse was about 3.5 mJ. Hydrodynamic simulations with the code Hydra²⁴ were used to
107 calculate the preplasma profile, as is shown in Figure 3(a).

108 Full 3D PIC simulations to model all physics processes are impractical with current super-
109 computers. We instead adopted a two-stage approach that has been demonstrated on other targets

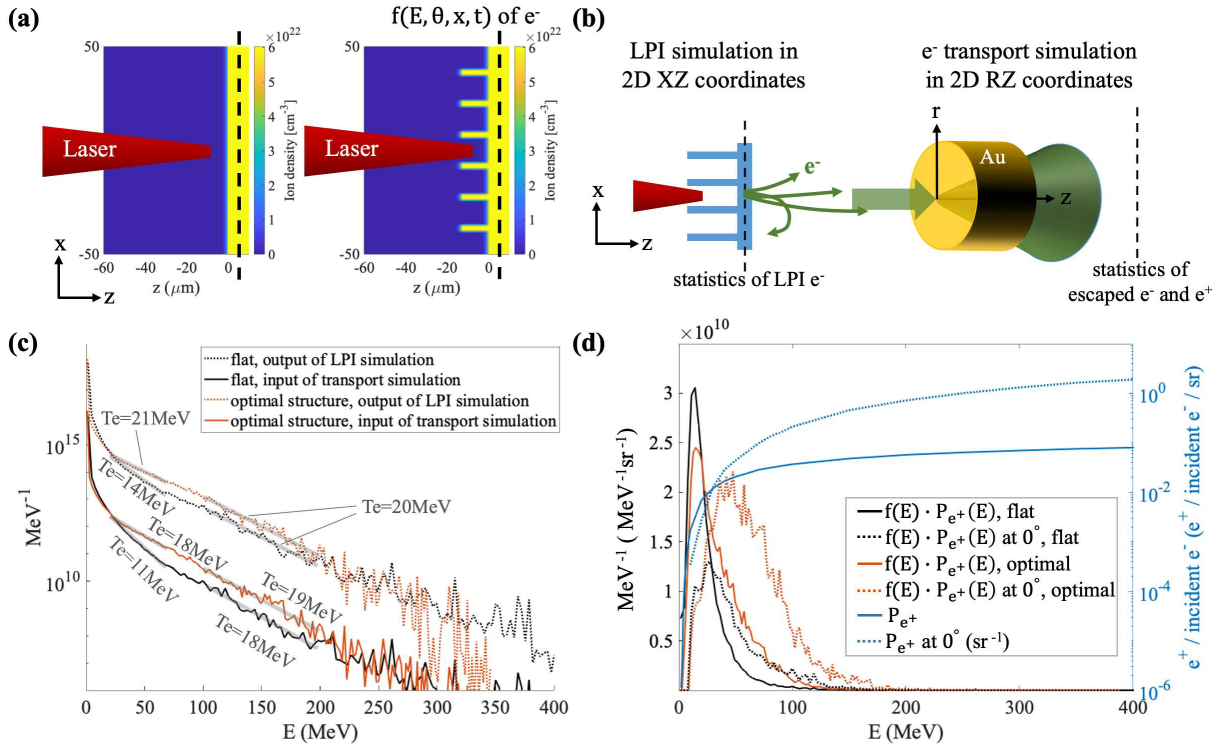


Figure 3: (a) Initial ion density for 2D Cartesian LPI simulations. (b) Schematic diagram of simulation setups. We have injected the fast electrons derived from LPI simulation to the following transport simulation after converting the electron source from Cartesian to cylindrical geometry. (c) Electron spectra inside the target from 2D Cartesian LPI simulations (dashed curves) and spectra of injected electron source for 2D cylindrical transport simulations (solid curves). (d) Solid blue curve (right y axis) shows the probability of one positron generated by one monoenergetic electron transporting through a 1mm thick, 1mm diameter Au target, and dashed blue curve shows the probability (per sr) of generating a positron that exits at 0° with respect to target normal. The black and red curves (with respect to the left y axis) show injection electron spectra multiplied by the positron generation probability as a function of energy.

110 ^{25,26} to simulate LPI and transport processes separately. The overall simulation process is illus-
111 trated in Figure 3(b). First a 2D Cartesian geometry was used to simulate the LPI process, with
112 only x and z dimensions modeled in space. However, the velocity was 3D as all 3 components v_x ,
113 v_y and v_z were updated at each time step. We could not use a cylindrical geometry because the
114 laser was linearly polarized in the x direction. The electrons were measured at a plane that was 5
115 μm inside the target. The energy, direction, position and time of each electron macroparticle have
116 all been recorded. We then processed the laser-generated electrons to get their distribution $f(E, \theta,$
117 $x, t)$ as a function of energy, angle, transverse distance, and time. Here the angle θ is defined as
118 $\cos^{-1}(v_z/v)$. At this point, we assumed a rotational symmetry (in ϕ) along the laser propagation
119 axis for both space and velocity, and converted the distribution to cylindrical coordinates so that $f(E,$
120 $\theta, r, t) = f(E, \theta, x, t)$. The transport simulation was performed in a 2D cylindrical geometry. When
121 hot electrons leave the target, they would create a strong sheath field on the back side. The sheath
122 field can slow down the electrons and cause reflux, as well as accelerate positrons. Therefore it is
123 critical to model the sheath field properly to obtain the correct yield and spectrum. The cylindrical
124 geometry is required to accurately model the $1/r^2$ fall-off of the E field, whereas the 2D Cartesian
125 geometry would result in a $1/r$ fall-off. The hot electrons were then re-sampled according to $f(E,$
126 $\theta, r, t)$ distribution and injected into a 1mm thick, 1mm diameter Au target in a 2D cylindrical
127 geometry. Positron generation and transport was then simulated both inside and behind the Au
128 target. To compare with the experimental results, statistics of escaped electrons and positrons were
129 performed at another extraction plane that was 2mm from the backside of the target.

130 The electron spectra generated from the LPI simulations are shown in Figure 3(c). The

131 dashed curves are the raw distributions derived in Cartesian coordinates and the solid curves are
132 converted distributions in cylindrical coordinates. The electron temperatures T_e for different por-
133 tions of the spectra are also labeled in the plot. After conversion, the temperature for higher-
134 energy-range electrons is maintained at around 20 MeV, which is quite close to the experimentally
135 measured temperature of 21 MeV. Lower energy electrons have a wider angular distribution and
136 thus tend to be more easily affected by the conversion. T_e decreased by about 3MeV for electrons
137 within 25 – 70 MeV. Comparing optimal structure (red) to flat (black), the main difference appears
138 at energies above 25 MeV, as the optimal structure tends to produce about an order of magnitude
139 more electrons within this energy range.

140 To evaluate the positron yield, in Figure 3(d) we have plotted $f(E) \cdot P_{e^+}(E)$, where $f(E)$ is
141 the spectrum of injected electrons (solid curves in Figure 3(c)), and $P_{e^+}(E)$ is the probability that
142 one positron could be generated and exit from the 1mm thick, 1mm diameter Au target as one inci-
143 dent electron with energy E is injected. $P_{e^+}(E)$ was obtained using a Monte Carlo code MCNP²⁷
144 and the field effects have been ignored. The results are shown as the blue solid curve in Figure
145 3(d) on a log scale. The positron production probability grows sharply with energy for incident
146 electrons below ~ 30 MeV and gradually saturates at high energies. The black and red solid curves
147 indicate the calculated $f(E) \cdot P_{e^+}(E)$ for flat and optimally structured targets, respectively. Both
148 curves peak at about 15 MeV. However, electrons within 25 – 150 MeV from the optimal structure
149 contributed to a great extent to the positron yield, whereas for the flat target most of the positrons
150 are generated by lower energy electrons. Overall, the injection spectrum from an optimally struc-
151 tured target produced about 30% more positrons than the flat target. Note that this estimation does

152 not consider any field or electron reflux effects that in reality play an important role. Higher energy
153 electrons also tend to produce more forward going positrons. Assuming that all injected electrons
154 have normal incidence, the dashed blue curve in Figure 3(d) shows the probability of one positron
155 exit at 0° from the backside of a Au target as one electron enters, i.e., positron per incident electron
156 per sr at 0° . Multiplying this probability by the injection electron spectra yields the two dashed
157 curves for flat (black) and optimally structured (red) targets, respectively. In this case, the peak
158 contribution shifts to higher energies: about 27 MeV for flat targets and 48 MeV for the optimized
159 structure. Moreover, the optimal structure generates about twice as many forward going positrons
160 at 0° angle as the flat target.

161 The Monte Carlo simulation only provides an intuitive view of the pair production capability
162 of LPI electrons. Understanding the energy difference in the measured positron spectra in contrast
163 requires closer evaluation of the transport PIC simulations that involve the sheath field. The com-
164 parison of modeled and experimentally measured positron spectra at target normal (laser direction)
165 is shown in Figure 4(a). The simulated spectra agree qualitatively with the experimental data. In
166 Figure 4(b), the dark solid curves show the simulated spectra of escaped electrons at 0° whereas for
167 comparison the light solid curves in the background show the corresponding experimental spec-
168 tra. Both spectra have a relatively good overlap within the energy range between 40 MeV and
169 110 MeV. At lower energy, the mismatch is expected because the experimentally measured spec-
170 tra include electrons that are generated at much later times than those covered by the simulation.
171 The simulated spectra showed less particles at high energies. However, according to Figure 3(d),
172 electrons above 110 MeV would make a negligible contribution to the positron yield. These high

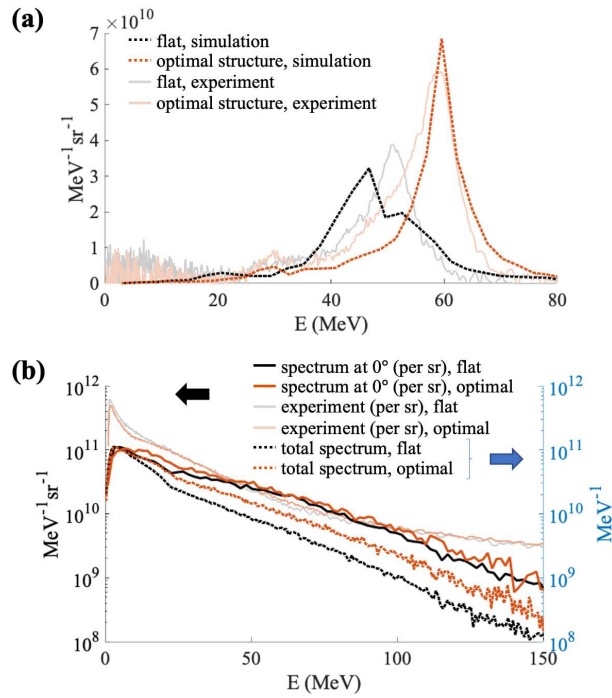


Figure 4: (a) Positron spectra at 0° from simulations. (b) Electron spectra at 0° (solid lines, with unit $\text{MeV}^{-1} \text{sr}^{-1}$ on the left y axis) and overall electron spectra (dashed lines, with unit MeV^{-1} on the right y axis). Note that the two different spectra plotted have mutually different units. We have also plotted corresponding experimental spectra at 0° in the background for comparison.

173 energy electrons have a small impact on the sheath field as well because their total charge is low.
174 Therefore, the simulated positron and electron spectra indicate that the injected electron source
175 from LPI simulation models the experimental condition reasonably well. For both the flat and the
176 optimally structured target, the electron spectra measured at the target normal direction are mutu-
177 ally quite similar, whereas the positron spectra are obviously different, in accord with experimental
178 observations. In Figure 4(b) we have also plotted the total electron spectrum (in MeV^{-1}) as the
179 dashed black and red curves. Unlike the spectra at 0° , the total spectrum from the optimally struc-
180 tured target clearly shows more high energy electrons, which explains the large discrepancy in the
181 positron spectra, because forward going positrons are generated by all electrons, not just by the
182 forward going ones.

183 The energy of positrons is largely determined by the sheath field on the back side of the
184 target. Figure 5 shows the evolution of the sheath field E_z as a function of the longitudinal position
185 z and time t . Column (a) are the results from the flat target and column (b) are from the optimally
186 structured target. Images (a1),(b1) and (a3),(b3) show the E_z field at $r=0$ and average E_z field
187 over the 1 mm diameter disk respectively, whereas (a2), (b2) and (a4), (b4) are the corresponding
188 voltages V calculated by integrating E_z over the longitudinal distance z . $V = \int_{z_0}^z E_z dz$, where $z_0 =$
189 1 mm indicates the back surface of the target. These plots allow for an estimate of the accelerating
190 capability of the sheath field. The images at $r = 0$, indicate that passes of electrons gradually
191 build up the sheath field on the target backside. Comparing the integrated voltage for flat and
192 optimally structured targets, both the voltage at $r = 0$ and the average voltage for the structured
193 target are about 10 MV higher than that for flat target, which is consistent with the measured

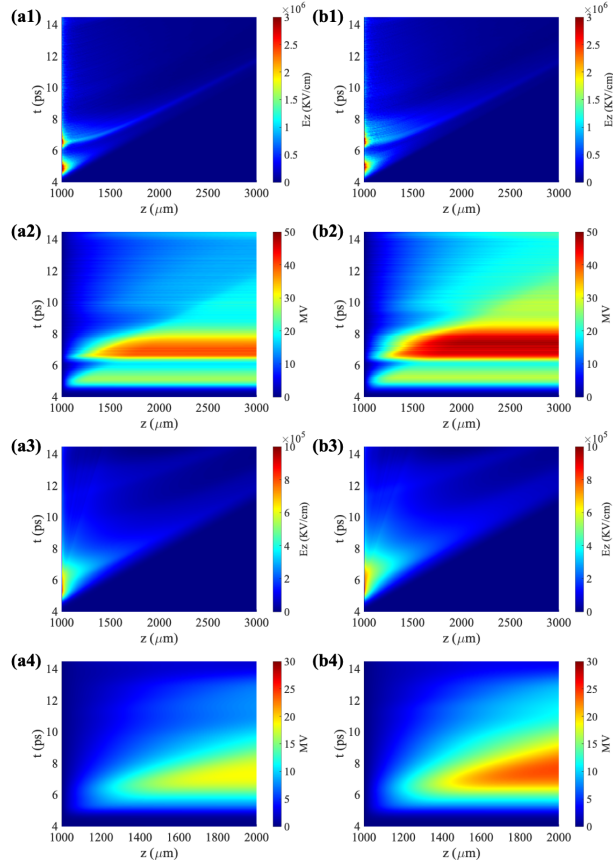


Figure 5: (a1), (b1) Sheath field E_z at $r = 0$ as a function of time and longitudinal position z . (a2), (b2) corresponding voltage calculated by integrating E_z over z . (a3), (b3) Average E_z over the back surface of the target. (a4), (b4) corresponding voltage by integrating the average E_z . Here column (a) is for flat target and column (b) is for optimally structured target.

194 energy difference between their positron peaks.

195 The two-stage PIC simulation successfully reproduced the experimental results, suggesting
196 its potential for further target structure optimization to control the generation of positrons and
197 other secondary particles, such as ions that are also greatly influenced by the sheath field. Optimal
198 target parameters will vary substantially with laser pulse length, intensity, focal spot size, and the
199 amount of prepulse. Nominally the wires need to be thick enough to survive the prepulse and the
200 rising edge of the main pulse, but not too thick to interfere with laser propagation. Therefore, the
201 desired diameter of wires increases with the laser pulse length and decreases with the laser contrast.
202 The wire length needs to be longer than the direct laser acceleration length so that the electrons
203 extracted from the wires by the laser can be accelerated to maximum speed. This acceleration
204 length is determined by the laser intensity and the preplasma density. There is usually a generous
205 range of wire lengths within which the wires would have a similar effect on the energy boost of
206 electrons. The optimal spacing between wires is determined by the focal spot size as well as the
207 scale of the preplasma. For high-energy, directional electron beam generation, the best result can
208 be achieved when the micro-structure spacing is similar to the size of the focal spot and when
209 a clean laser pulse is used. In contrast, reducing the structure spacing and introducing a proper
210 amount of preplasma can enhance laser absorption. Therefore a compromise between the two
211 effects has to be reached to maximize pair production.

212 The number of LPI electrons that are 10s of MeV or higher determines the number of
213 positrons that can be generated inside the convertor target as well as the charge that can escape

214 from the target that subsequently determines the sheath field. For a given convertor target, e.g.
 215 1 mm Au, the positron generation probability increases slowly for electrons above ~ 40 MeV
 216 according to Figure 3(d), and according to Figure 5, any electron that is above ~ 50 MeV can
 217 escape from the target. Therefore unlike previous work that used the structures for relativis-
 218 tic electron beam generation^{17,18}, our goal here is not to accelerate the electrons to the highest
 219 possible energy, but to generate as many moderate energy (10s of MeV) electrons as possible
 220 without sacrificing the laser conversion efficiency. Having a proper amount of preplasma is ben-
 221 eficial in our application. The current experiment was performed with a prepulse that naturally
 222 existed in the OMEGA EP laser. Future experiments with a controlled prepulse may further im-
 223 prove the positron yield. Another potential advantage of using the target structures is that the
 224 positron yield and energy are more sensitive to the laser intensity. The temperature T_e of fast
 225 LPI electrons near the critical density can usually be estimated using the ponderomotive scaling
 226 $T_e \approx 0.511 \times (\sqrt{1 + I(W/cm^2)\lambda^2/1.4 \times 10^{18}} - 1) \text{ MeV}$ ²⁸, and for high intensity, T_e approximately
 227 grows like the square root of the intensity. However, with the microwire array, the highest-energy
 228 electrons are accelerated via a different direct laser acceleration mechanism. The energy of this
 229 particular portion of the electrons scales linearly with laser intensity. Consequently, the positrons
 230 that are generated by them also tend to have a stronger dependence on intensity. Therefore the
 231 structured target would be more advantageous if higher-intensity lasers are developed in the fu-
 232 ture. Our PIC simulations have shown that even the “hot spot” in the laser focal spot cannot be
 233 ignored and is important to the resultant energy and number of positrons.

234 **Conclusions**

235 In summary, front surface target structures have been shown experimentally to substantially en-
236 hance the positron yield and energy for the first time, constituting a cost-effective approach to
237 use laser-generated positron sources for laboratory astrophysics applications. The follow-up sim-
238 ulations explain the entire process of how the laser-plasma interaction that is manipulated by the
239 target structure affects the yield and energy of positrons. The agreement between the simulated
240 and experimental spectra indicates the possibility of further target optimization using two-stage
241 PIC simulations.

242 **References**

- 243 1. Piran, T. *Rev. Mod. Phys.* **76**, 1143 (2005).
- 245 2. Chen, H. *et al. High Energy Density Physics* **7**, 225 (2011).
- 246 3. Liang, E. *et al. Sci. Report* **5**, 13968 (2015).
- 247 4. Sarri, G. *et al. Nat. Comm.* **6**, 6747 (2015).
- 248 5. Stoneking, M., Pedersen, T., Helander, P. *et al.* A new frontier in laboratory physics: electron-
249 positron plasmas. To be published.
- 250 6. Schwinger, J. *Phys. Rev.* **82**, 664 (1951).
- 251 7. Breit, G. & Wheeler, J. A. *Phys. Rev.* **46**, 1087 (1934).

- 252 8. Bell, A. R. & Kirk, J. G. *Phys. Rev. Lett.* **101**, 200403 (2008).
- 253 9. Sarri, G. *et al.* *Phys. Rev. Lett.* **110**, 255002 (2003).
- 254 10. Chen, H. *et al.* *Phys. Rev. Lett.* **105**, 015003 (2010).
- 255 11. Chen, H. *et al.* *Phys. Plasmas* **21**, 040703 (2014).
- 256 12. Chen, H. *et al.* *Phys. Rev. Lett.* **114**, 215001 (2015).
- 257 13. Xu, T. *et al.* *Phys. Plasmas* **23**, 033109 (2016).
- 258 14. Williams, G. J. *et al.* *Phys. Plasmas* **23**, 123109 (2016).
- 259 15. Yan, Y. *et al.* *Plasma Phys. Control. Fusion* **59**, 045015 (2017).
- 260 16. Bethe, H. & Heitler, W. *Proc. Royal Soc. of London A* **146**, 83 (1934).
- 261 17. Jiang, S. *et al.* *Phys. Rev. Lett.* **116**, 085002 (2016).
- 262 18. Jiang, S., Krygier, A. G., Schumacher, D. W., Akli, K. U. & Freeman, R. R. *Phys. Rev. E* **89**,
263 013106 (2014).
- 264 19. Jiang, S., Krygier, A. G., Schumacher, D. W., Akli, K. U. & Freeman, R. R. *Eur. Phys. J. D*
265 **68**, 283 (2014).
- 266 20. Chicago is being developed by Voss Scientific with partial support from the Defense Advanced
267 Research Projects Agency under Contract No. W31P4Q-15-C-0055 and the Air Force Office
268 of Scientific Research under Contract No. FA9550-14-C-0034.

- 269 21. Warren, E. L., Atwater, H. A. & Lewis, N. S. *J. Phys. Chem. C* **118**, 747 (2014).
- 270 22. Henry, M., Welch, C. & Scherer, A. *J. Vac. Sc. Technol. A* **27**, 1211 (2009).
- 271 23. Dorrer, C., Consentino, A., Irwin, D., Qiao, J. & Zuegel, J. D. *J. Opt.* **17**, 094007 (2015).
- 272 24. Marinak, M. M. *et al. Phys. Plasmas* **8** (2001).
- 273 25. Bartal, T. *et al. nature phys.* **8**, 139 (2011).
- 274 26. Sawada, H. *et al. Phys. Plasmas* **19**, 103108 (2012).
- 275 27. Los Alamos Scientific Laboratory. Group X-6. MCNP : a General Monte Carlo Code for
276 Neutron and Photon Transport. Los Alamos, N.M. : [Springfield, Va.] :Dept. of Energy, Los
277 Alamos Scientific Laboratory ; [for sale by the National Technical Information Service], 1979.
- 278 28. Wilks, S. C., Kruer, W. L., Tabak, M. & Langdon, A. B. *Phys. Rev. Lett.* **69**, 1383 (1992).

279 **Acknowledgements** We thank the OMEFA EP team for laser operation and technical support. This work
280 was performed under the auspices of the U.S. DOE by LLNL under Contract DEAC5207NA27344, and
281 funded by LDRD (#17ERD010). The fabrication of Si microwire arrays was supported through the Office
282 of Science of the U.S. Department of Energy under Award No. DE- SC0004993. Additional support for this
283 work was provided by the Lockheed Martin Corporation (Award 4103810021). We thank the staff at the
284 Kavli Nanoscience Institute at Caltech for their technical assistance with fabrication.

285 **Competing Interests** The authors declare that they have no competing financial interests.

286 **Correspondence** Correspondence and requests for materials should be addressed to S. Jiang (email:
287 jiang8@llnl.gov) or H. Chen (email: chen33@llnl.gov).

Figures

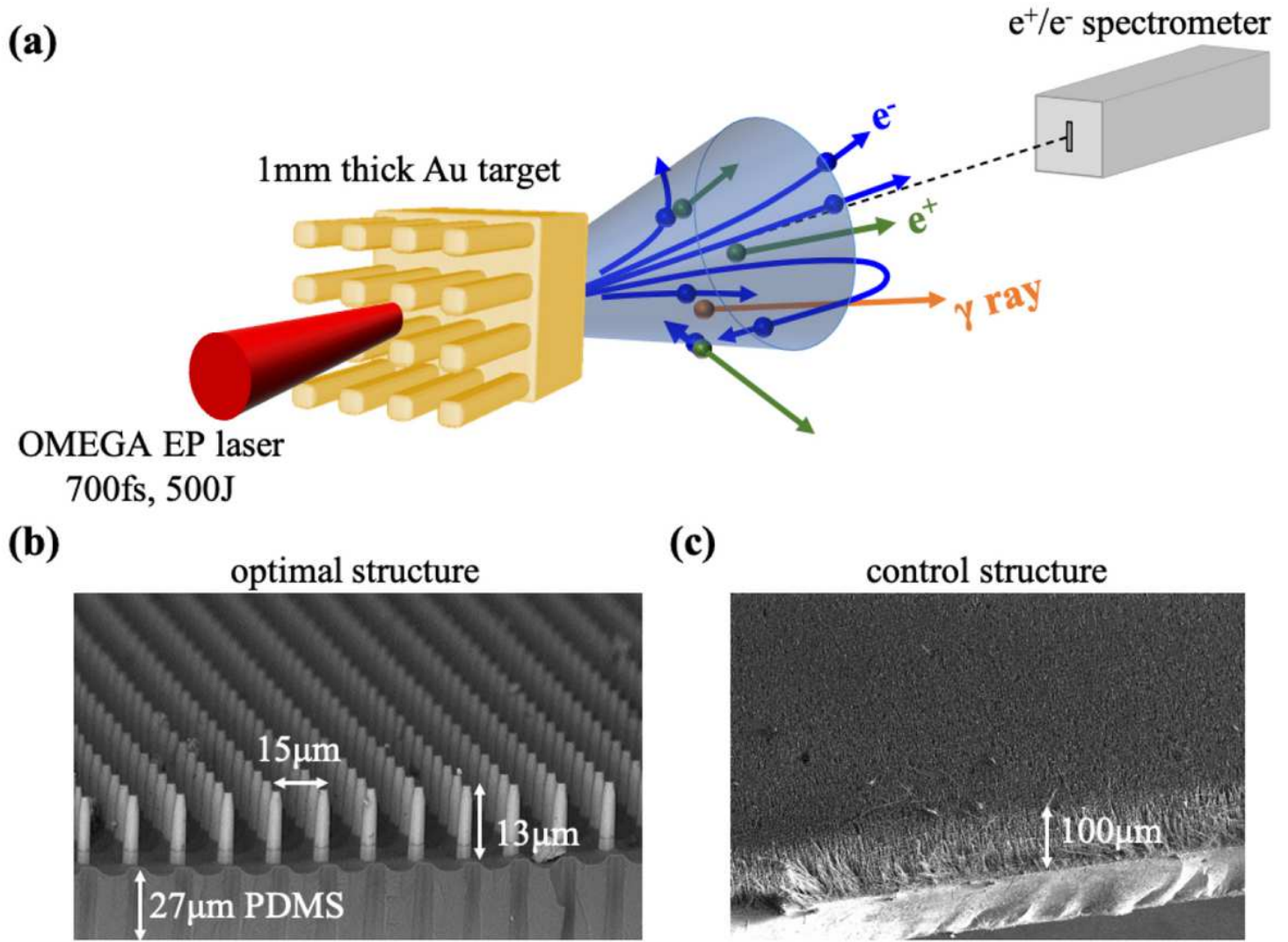


Figure 1

Schematic diagram of the experimental setup and scanning electron microscope (SEM) images of targets. (a) Schematic of the experimental setup. The same setup is used for LPI PIC simulations. The laser has 500 J energy, 700 fs pulse length and a peak intensity of 4.46×10^{20} W/cm². Target structures are made of Si wires that reside on a thin piece of polydimethylsiloxane. They are then attached to a 1mm thick Au convertor target for positron generation. The electron/ positron spectrometer is placed opposite to the laser pulse. (b) SEM image of the optimized target structure. The wires are 3 μm in diameter and 15 μm apart. They have a total length of 40 μm but their bottom parts are embedded inside a 27 μm polydimethylsiloxane layer; therefore the wire structures exposed outside the polydimethylsiloxane is 13 μm . (c) SEM image of the unoptimized control structure used in the experiment. The Si wire array is about 100 μm long (exposed outside polydimethylsiloxane), 3 μm in diameter, and 7 μm in period.

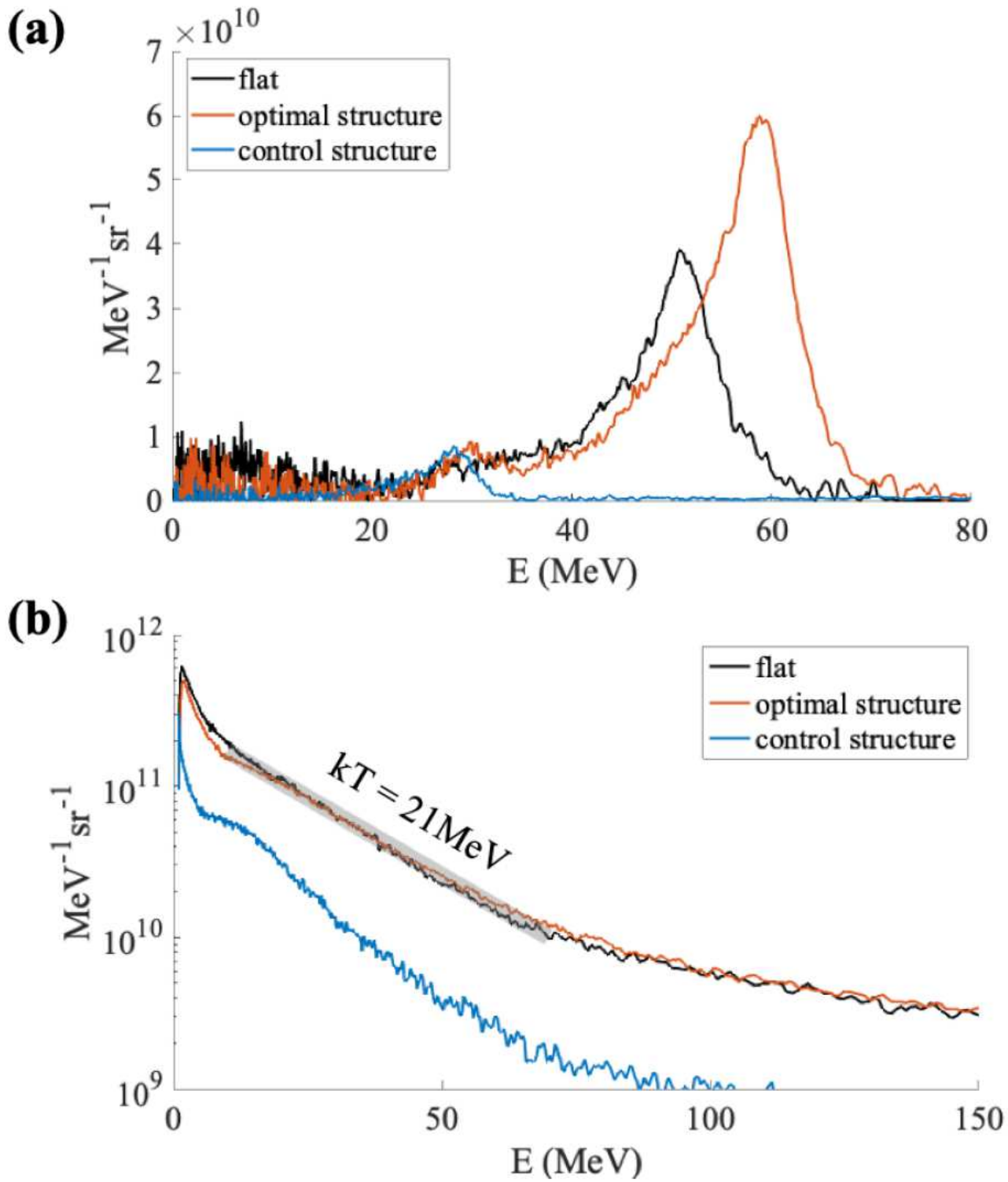


Figure 2

Experimentally measured spectra for (a) positrons and (b) electrons. Different colors indicate the results from different targets under the same laser conditions.

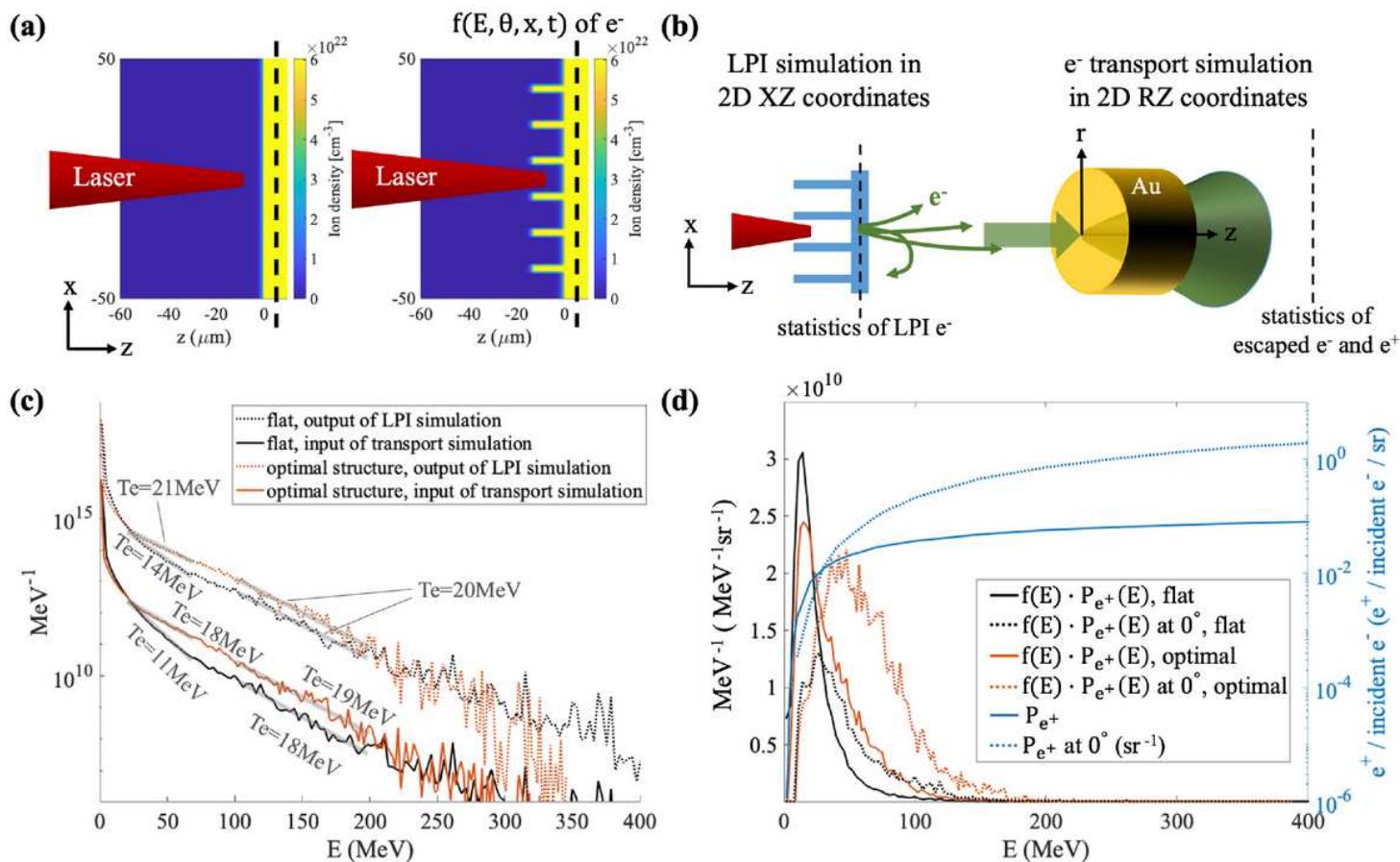


Figure 3

(a) Initial ion density for 2D Cartesian LPI simulations. (b) Schematic diagram of simulation setups. We have injected the fast electrons derived from LPI simulation into the following transport simulation after converting the electron source from Cartesian to cylindrical geometry. (c) Electron spectra inside the target from 2D Cartesian LPI simulations (dashed curves) and spectra of injected electron source for 2D cylindrical transport simulations (solid curves). (d) Solid blue curve (right y axis) shows the probability of one positron generated by one monoenergetic electron transporting through a 1mm thick, 1mm diameter Au target, and dashed blue curve shows the probability (per sr) of generating a positron that exits at 0° with respect to target normal. The black and red curves (with respect to the left y axis) show injection electron spectra multiplied by the positron generation probability as a function of energy.

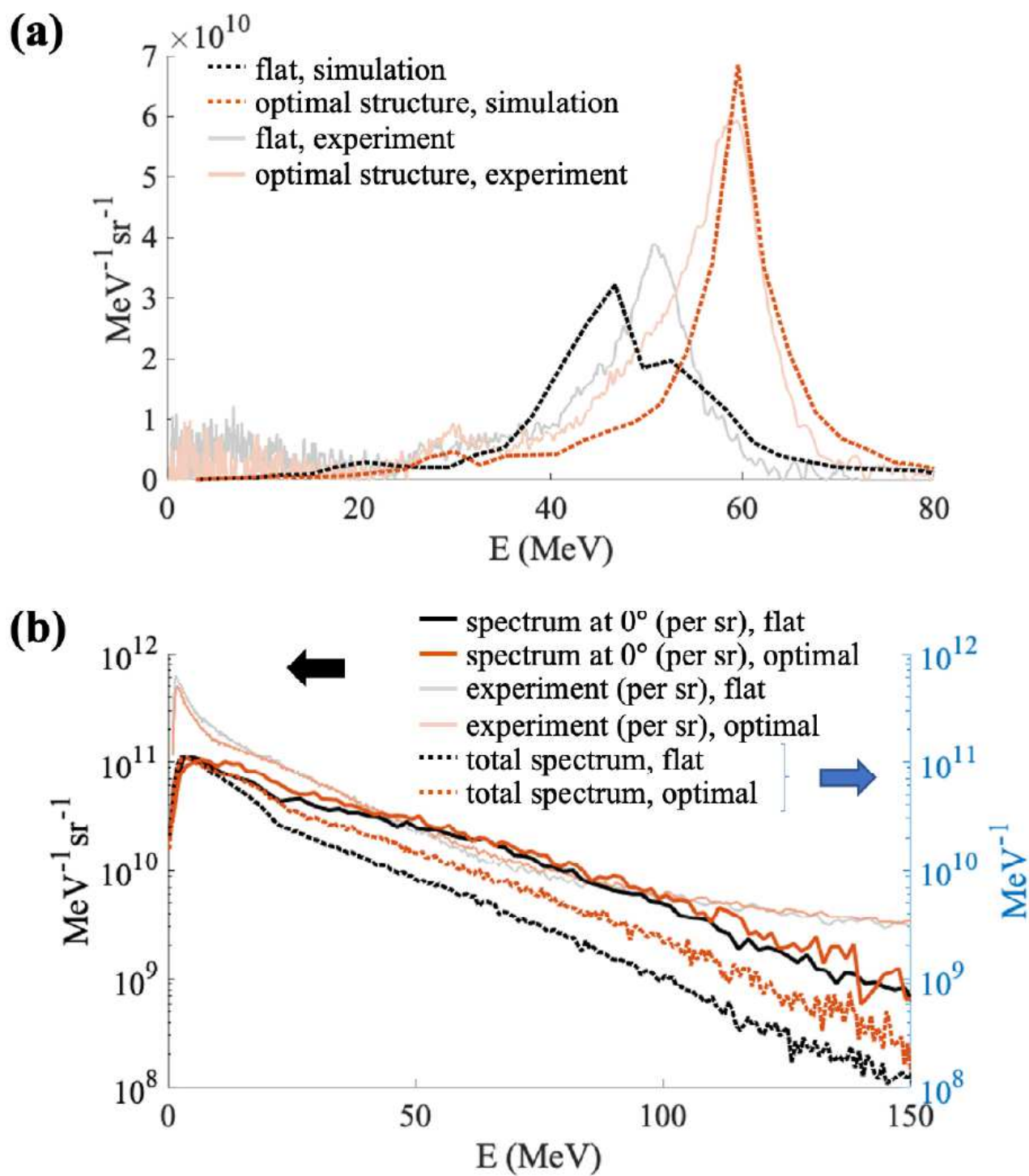


Figure 4

(a) Positron spectra at 0° from simulations. (b) Electron spectra at 0° (solid lines, with unit $\text{MeV}^{-1} \text{sr}^{-1}$ on the left y axis) and overall electron spectra (dashed lines, with unit MeV^{-1} on the right y axis). Note that the two different spectra plotted have mutually different units. We have also plotted corresponding experimental spectra at 0° in the background for comparison.

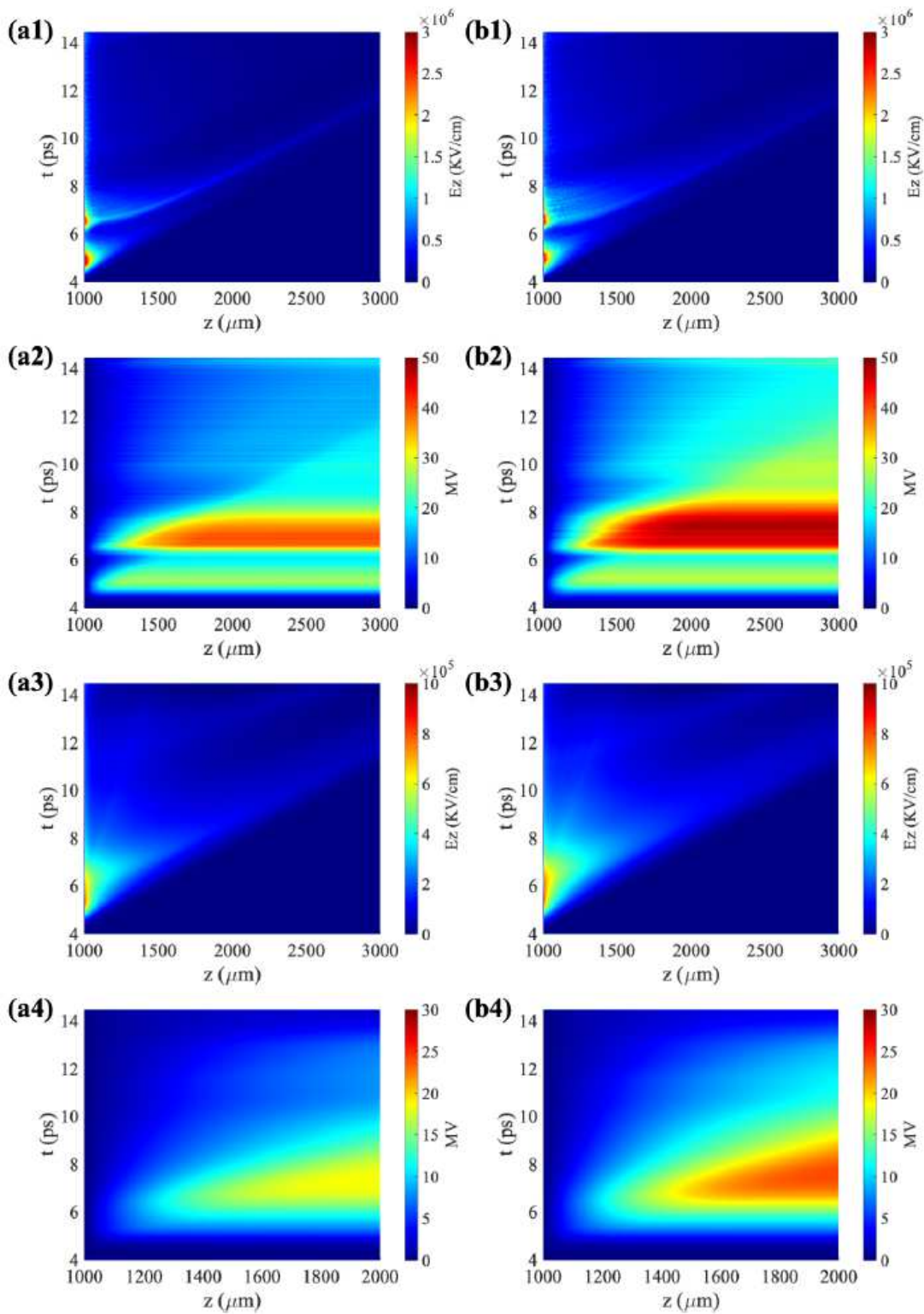


Figure 5

(a1), (b1) Sheath field E_z at $r = 0$ as a function of time and longitudinal position z . (a2), (b2) corresponding voltage calculated by integrating E_z over z . (a3), (b3) Average E_z over the back surface of the target. (a4), (b4) corresponding voltage by integrating the average E_z . Here column (a) is for flat target and column (b) is for optimally structured target.